Probing the partitioning behaviour of Xe using in situ X-ray synchrotron techniques at high P–T conditions

Qi Chen, Chrystèle Sanloup, Hélène Bureau, Igor Rzeplinski, Konstantin Glazyrin, Robert Farla

Probing the partitioning behaviour of Xe using *in situ* X-ray synchrotron techniques at high *P-T* conditions

Qi Chen[a*], Chrystèle Sanloup[a], Hélène Bureau[a], Igor Rzeplinski[a], Konstantin Glazyrin[b] and Robert Farla[b]

[a]Sorbonne Université, CNRS, MNHN, Institut de Minéralogie, de Physique des Matériaux et de Cosmochimie, 4 place Jussieu, 75252 Paris, France

[b]Photon Science, Deutsches Elektronen-Synchrotron, D-22607, Hamburg, Germany

Probing the partitioning behaviour of Xe using *in situ* X-ray synchrotron techniques at high *P-T* conditions

Abstract

Understanding crystal/melt xenon (Xe) partitioning at depth is key to properly trace planetary processes using Xe isotopes. Partition coefficients measured on experimental samples recovered at room pressure (*P*) and temperature (*T*) span six orders of magnitude, potentially due to Xe exsolution from crystals upon quenching. We chose two *in situ* synchrotron X-ray methods to investigate Xe crystal/melt partitioning under high *P* and *T* up to 3 GPa and 1050 °C using (1) resistive-heated diamond anvil cell with angle-dispersive diffraction and X-ray fluorescence, and (2) a new protocol using large volume press with energy-dispersive diffraction set-up. Results from both methods are consistent, and Xe is found to be compatible at depth, suggesting the continental crust could be a Xe-rich reservoir.

This new protocol advances research to probe geological systems at the higher *P-T* conditions accessible with large volume press while maintaining homogeneous *T* throughout the sample.

1. Introduction

Noble gases, which have been extensively studied by geoscientists, play a key role to track several processes in Earth and planetary sciences, ranging from planetary and atmosphere formation [1,2], mantle convection [3,4] and tracking underground nuclear tests [5]. However, Xe stands out amongst other heavy noble gases as it is strongly depleted relative to chondritic patterns. Up to 90% Earth's and Mars' Xe is missing from the atmosphere, which is known as the 'missing Xe paradox' [6,7]. This issue has become one of the most challenging riddles in the planetary sciences for decades. Xenon could have escaped from the atmosphere [8,9], and/or could be trapped at depth. The latter scenario is supported by the demonstration of Xe reactivity at much lower pressures as a trace/minor element with planetary materials such as olivine and quartz, through the formation of Xe-O bonds [10-12], also evidenced in deep crustal melts [13].

However, there are still many fundamental unknowns about the chemical behaviour of Xe with planetary materials. To better constrain Xe distribution, one of the most effective ways is to investigate the partition coefficients between major silicate minerals and melts in melting and crystallizing processes. *Ex situ* measurements of partition coefficients of Xe ($D^{Xe}_{crystal/melt}$) on quenched samples span over 6 orders of magnitude (*e.g.*, 6×10^{-4} to 350 for olivine/melt partitioning) from ambient *P* to 1.5 GPa and 1000-1300 ºC [14-16]. However, Xe is found partly located in gas bubbles in these samples, resulting in inconsistencies in Xe solubility and partition coefficients whether or not bubbles are analyzed, *i.e*. whether or not bubbles reflect equilibrium at high *P-T* or are produced upon quenching the experiment back to room conditions.

Therefore, it is questionable whether the measured solubility and partition coefficient faithfully reflect the equilibrium solubility and partition coefficient at experimental high *P-T* conditions. Consequently, it is essential to carry out *in situ* measurements at high *P* and *T* to evaluate partitioning of volatile elements such as Xe at depth. First *in situ* partitioning experiments between aqueous fluids and haplogranitic melt ($D^{Xe}_{f/m}$) under high *P* showed that Xe degassing is strongly *T*-dependent, varying from 2750 to 0.15 in the range of 680 to 850 ºC [13], indicating that Xe is preferentially retained in deep crust melts in hot contexts but otherwise very efficiently degassed in the fluid.

There are so far no *in situ* measurements on Xe crystal/melt partitioning at depth. Here we present a method to investigate partitioning of Xe in crystal/melt system using large volume press (LVP) with *in situ* synchrotron energy dispersive set-up (EDX), which allows simultaneous collection of diffraction and fluorescence signal under high *P-T*. To demonstrate the feasibility of this technique, we also conducted experiments using the more established combination of resistive-heating diamond anvil cell (DAC) with *in situ* synchrotron angle dispersive X-ray diffraction (ADX) and X-ray fluorescence analysis (XRF). Experimental data were collected up to 3 GPa and 1050 °C (Table 1), the maximum *T* achievable using our resistive-heating DACs. We consequently focussed this first investigation of Xe crystal/melt partitioning on a silica-rich hydrated composition which liquidus is relatively low, co-existing with either plagioclase or clinopyroxene (jadeite or omphacite, cf Table 1). This melt composition is a good analogue of continental crust melts, while plagioclase and clinopyroxene are two main rock-forming minerals making up the Earth's crust [17].

2. Methods

2.1 Synthesis of starting glasses

Starting glasses were prepared from reagent grade carbonates (Na_2CO_3 and $CaCO_3$) and oxides (Al_2O_3 and SiO_2) powders with a nominal composition of 80/20 mol% albite/anorthite ($Ab_{80}An_{20}$). Powders were firstly ground and decarbonated by slowly heating in a platinum (Pt) crucible in an atmospheric furnace from room *T* to 1000 °C, run for 10 hours, molten at 1650 °C for 1 hour, and then quenched in water. Recovered glass was crushed into powder again, and remolten twice to ensure homogeneity.

For hydration and Xe doping processes, recovered $Ab_{80}An_{20}$ glass was first loaded into one-end welded Pt capsule to which were added 12 wt% water, and Xe using a gas loading device [18]. The capsule was brought to 2 GPa and 1500 °C using a piston-cylinder apparatus with a half-inch talc pyrex assembly, a graphite heater, and dried MgO powder packed around the Pt capsule, followed by rapid *T* quenching and decompression at room *T*. To assess the potential effect of Xe content on its distribution, glasses with two different Xe contents were used, 0.14 wt% and 0.02 wt% respectively (Table 2), which are far less than Xe solubility (0.32-0.41 wt%) measured in tholeiitic melt at 1.5-2 GPa [19]. There are no available data on Xe solubility in albite-anorthite melts. However, knowing that noble gases solubility increases with SiO_2 melt content [20], our experiments are well below Xe-saturated condition.

For DAC experiments, only few pieces of starting glass were needed. For large volume press experiments, more starting glass was extracted from the Pt capsule as

larger amounts of sample were needed, which accidentally brought some MgO packed outside the Pt capsule into the sample, resulting in growth of clinopyroxene omphacite at high *P* (see section 2.5 and Table 1).

2.2 Diamond-anvil cell experiments with angle-dispersive set-up

Symmetric large opening DACs (70°) equipped with Boelher-Almax seats and 800 μm diameter culet diamonds were used to generate high *P-T* conditions [21]. Laser drilled Re gasket was used as sample chamber (250 μm diameter) filled with Xe-doped hydrous plagioclase glass. Resistive-heating was achieved using the internal heating technique developed by Fei and Mao [22] modifier by using a Pt wire. *T* was recorded by a type S thermocouple located on the edge of the gasket closed to the sample chamber. Pressure at ambient *T* was measured by ruby fluorescence, and was monitored at high *T* from the cell volume of a piece of gold [23] inserted in the sample chamber. A schematic of the resistive-heating DAC assembly is given in supplementary information (Fig.S1).

Synchrotron experiments were performed at the beamline P02.2, Petra III (DESY, Hamburg) using a 3×8 mm^2 focused monochromatic X-ray beam at 42.7 keV, following the same strategy as in previous studies [13,24]. At each *T* step, ADX patterns were recorded on a CsI bonded amorphous silicon detector (Perkin Elmer XRD 1621) to identify phases (*i.e.*, crystalline *vs* molten) and monitor *P* from the cell volume of the Au internal calibrant. The X-ray diffraction patterns were integrated from the images with Fit2D software [25], and the diffraction signal was Le Bail fitted using Fullprof software [26] to obtain phase identification, crystal cell-volume,

and melt fraction for melt + crystals data-sets. XRF signal was collected on a Vortex® 60-EX silicon drift detector with a collection time of 900-1800 s.

2.3 Large-volume press experiments with energy-dispersive set-up

High *P-T* experiments were carried out using a Hall-type press equipped with 6 hydraulic rams (mavo press LPQ6-1500-100 by Voggenreiter) at the P61B LVP-EC beamline, PETRA III (DESY, Hamburg), using a combination of 6 first-stage anvils and 8 tungsten carbide (WC) second-stage anvils. We used the 18/11 cell-assembly with truncated edge lengths of 11 mm, doped octahedra MgO with a graphite heater, ZrO_2 thermal isolator and MgO as the capsule container (supplementary information Fig. S2). Temperature was monitored using a type C thermocouple. To preserve the sample chemical integrity and cylindrical geometry while being transparent to X-rays, diamond cylinder (2 mm height x 1 mm inner diameter) was used as sample capsule sealed under *P* by platinum-rhodium caps.

Energy-dispersive diffraction and fluorescence signals were collected using a low energy Germanium detector (LEGe) and a diffracted beam collimated to 50×300 μm^2. The radiographic imaging system is composed of a GGG:Eu scintillator (40 µm thickness), an objective lens with 5x magnification, a mirror and a sCMOS camera. The scattering angle 2θ was calibrated by measuring MgO each time before compression, which remained constant at 7.1312° ± 0.0003°. Based on the detector position and the incident beam and collimator slits size (both 50×300 μm^2), the maximum size of the gauge volume from where the diffracted X-rays were collected in the sample is no larger than 0.03 mm^3. Pressure was derived from the equation of state of MgO [27] by recording its diffraction pattern (MgO cylinder surrounding the

sample capsule) before and after each measurement on sample to ensure that *P* was kept constant. In case the thermocouple broke down during experiments, *T* was then determined using the power *vs T* calibration curve established before failure (supplementary information Fig. S3). Experimental conditions are reported in Table 1. EDX data were collected for 60 seconds for both MgO and sample, and data collection was iterated a large number of times (50-175) on the sample at the same position and averaged to optimize the signal to noise ratio for the Xe fluorescence peaks. For run HH357, the pyrophyllite gaskets on the anvils were modified with boron-epoxy windows to reduce X-ray absorption for both the incident and diffracted X-rays. Explored *P-T* conditions along with observed phases are summarized in Table 1.

2.4 X-ray tomography on recovered large volume press samples

For X-ray diffraction patterns that display a mixture of crystalline and molten phases (Table 1), it is necessary to determine the phases fractions to constrain Xe partitioning. This can be obtained in the case of LVP experiments from fitting the melt fraction on diffraction data (see section 3.2), and was cross checked by carrying X-ray tomography scans on two recovered samples. For this purpose, the diamond capsule, still containing the sample, was extracted from two recovered cell-assemblies after the experiments. The cell-assembly is indeed very absorbing which impedes the detection of absorption contrast between crystals and melt *in situ* at high *P-T* conditions.

X-ray tomography scans were done at the micro-CT scan facilities at the National Museum of Natural History in Paris (AST-RX platform). The voltage used was 160 kV, and the power on sample was 10 W. Detector size was 400 × 400 mm^2 with a

2024×2024 pixels matrix. The voxel size was approximately 2 µm, with an acquisition time of 2 seconds per frame.

2.5 Chemical analyses

Quenched samples together with starting glasses were put in epoxy resin and polished for Raman analysis, scanning electron microscopy, and electron microprobe analyses. A Zeiss Ultra 55 field emission scanning electron microscope (SEM) was used with a working distance of 7.5 mm and a voltage of 20 kV for detection of Xe. Major elements were analyzed using a Cameca SX-FIVE electron microprobe analyzer (EPMA) on the Camparis platform. The beam was focused to 15 µm diameter on the sample. Conditions were set to 15 kV acceleration voltage, 5 nA beam current, and 10 s counting time per element on both peak and background for Na, Ca, Al, Si, and 15 kV, 40 nA, and 60 s counting time on Xe peak and 30 s on background. Xenon calibration was established following the procedure developed by Montana et al. [28] by measuring the counts for the neighbouring elements, I (CuI) and Cs (CsCl). This method had been previously confirmed by analyzing one Xe-bearing glass PC53 (2.6 wt% Xe; haplogranite glass from C. Crépisson's PhD thesis [30]), for which Xe content was assessed by Particle induced X-ray emission [29].

All analyses are summarized in Table 2. Based on SEM and EPMA analyses, the synthesized starting glass $Ab_{80}An_{20}$ is chemically homogeneous. Low Na_2O content likely is an artefact caused by Na loss during EPMA analysis, and the relatively low total may account for Na loss. The numerous lighter roundish zones observed by SEM in PC162a and b are too tiny to get quantitative insights (Fig. 1a and 1b), but are most likely Ca-rich seeds, Ca being the only major heavier element.

To constrain H_2O content in starting and recovered glasses, Raman spectra were recorded on a Jobin-Yvon Horiba HR460 spectrometer using a single-grating monochromator with 1500 gratings/mm and an argon laser (514.5 nm wavelength) with the power of 11.4 mW. All spectra were acquired at room *T* with accumulation time of twice 45 s. For LVP experiments, H_2O content determined using is similar within the uncertainties in starting and quenched glasses (see supplementary text and Fig.S4), attesting that the sample remained sealed. However, H_2O losses were found for DAC experiments, which must have occurred during the quenching process because if H_2O had been lost during experiments, no melt should have been detected at experimental *T* based on hydrous albite phase diagram [30].

Note that MgO is detected in quenched phases from LVP experiments (samples HH355 and HH357) resulting in growth of clinopyroxene due to the MgO contamination before *in situ* high *P-T* experiments (Table 2 and section 2.1). Recovered clinopyroxene crystals from LVP experiments were caracterized by Raman spectroscopy (supplementary Fig.S5) and SEM analyses showing calcic-magnesic cores and more sodic rims (Fig. 1d to 1f). This indicates that the contamination of MgO results in the transformation of albite ($NaAlSi_3O_8$)-anorthite ($CaAl_2Si_2O_8$) join to jadeite ($NaAlSi_2O_6$)-omphacite ($(CaNa)(MgAl)Si_2O_6$) join at high *P* [31], also confirmed by the observation of additional alumina silicate (Al_2SiO_5) in recovered sample HH357 (Fig. 1f). No Xe is detected in the quenched crystals, although a few bubbles open upon polishing are observed inside crystals (Fig. 1e and 1g). Chemical analyses show that the inclusion in the middle of clinopyroxene crystals (Fig. 1f) has the same composition as the melt.

In addition to H_2O, CH_4 vibrational modes are detected in the quenched glass by Raman spectroscopy (supplementary Fig.S3). Holes observed in recovered sample HH355 (Fig. 1d and 1e) thus are assumed to be exsolution of CH_4 produced at experimental conditions by reaction with the diamond capsule, also attested by the presence of some graphite crystals in the glass in one run (Fig. 1f and 1g).

3. Xe crystal/melt partitioning measurements

3.1 In situ determination of Xe content in crystals and melt

For large volume press experiments, after a first compression step, *T* was initially increased until full melting was reached to ensure equilibrium, then decreased stepwise until both crystalline and molten phases co-exist, and hold for 1800 s before data collection. For resistive-heating DAC experiments, full melting was almost reached, with some crystals nonetheless preserved on the edge of gasket (Fig. 1c).

While it is difficult to distinguish crystals *vs* melt from visual observations (DAC experiments) or *in situ* radiographic imaging (LVP experiments), X-ray diffraction allows unambiguous phase determination (Fig. 2a and 3). Therefore, at the targeted *P-T* conditions, samples were scanned while collecting X-ray diffraction data until best positions were found: one optimizing crystalline diffraction signal (further referred as 'crystal-rich'), and one optimizing melt diffuse signal (further referred as 'melt-rich') with eventually pure melt.

At each position, Xe content is determined using the fluorescence signal of Xe K_α line (29.78 keV) either on a specific fluorescence detector for angle-dispersive set-up (DAC experiments) or on the same detector used for diffraction for energy-dispersive

set-up (LVP experiments). While Xe K_β line is visible at 33.62 keV, the weak signal/ noise ratio prohibits its use for determination of Xe content.

For angle-dispersive DAC experiments, energy calibration and quantification of Xe content from signal intensity were calibrated *in situ* in the DAC at room conditions by filling a gasket with a Xe-doped glass PC53 (2.6 wt% Xe; unpublished data, haplogranite glass from C. Crépisson's PhD thesis [32]) previously analyzed by both EPMA and Particle X-ray Emission [29]. XRF data are processed with PyMCA software with the declaration of attenuation by absorption of Be window and diamond anvils [33]. At 1010 °C, melt proportion (see section 3.2 for determination of phases fractions) is more than 97% in the 'melt-rich' pattern thus we assume it can represent the Xe content in pure melt (Table 3). As for 'crystal-rich' pattern which contains a mixture of crystals and melt, data are further treated in a multilayer way. We assume there are two layers (melt and crystalline) in 'crystal-rich' pattern, sample thickness is assumed to be equal to that of the recovered gasket and proportions are taken as the relative layer thickness. Xenon content in crystals is then obtained from mass balance calculation in PyMCA software, as the bulk Xe content of the starting glass before heating is known and Xe content in the melt is taken from the 97% melt-rich pattern.

Fluorescence peaks on energy-dispersive patterns from LVP experiments are fitted following Simabuco and Nascimento [34] whereby the absolute intensity of the fluorescence signal depends on the five following factors: 1) beam intensity, 2) Xe concentration in the sample, 3) volume of the sample probed by X-rays, 4) absorption by the sample and the surrounding cell-assembly, 5) detector sensitivity. Note that these underlying physics are the same as implemented in the PyMCA software used above. They can be expressed by:

$$I_i = Xe_i \times \rho_i \times S \times D_i \times I_i^0 \times 10^{-A} \quad (1)$$

where Xe_i is Xe weight fraction in the volume probed by X-rays at a given position i; ρ_i, the average density; D_i, the sample thickness along X-ray beam path; S, the X-ray sensitivity of the spectrometer; I_i^0, the total beam intensity; A, the absorption by the sample and the surrounding cell-assembly.

As we know the Xe content in the starting sample, the $S \times I_i^0 \times 10^{-A}$ product can be calculated (cf equation 1) from Xe K_α fluorescence peak intensity collected at high P at the highest T while the sample is fully molten. We specifically used diamond capsules as those do not deform under our P-T conditions hence the path length, D_i, through the sample remains constant.

Assuming that the intensity of Xe K_α fluorescence peak can be expressed by the peak area, Xe_i can be written as:

$$Xe_i = Xe_{starting\ glass} \times \frac{peak\ area\ at\ position\ i}{peak\ area\ for\ starting\ glass} \times \frac{\rho_{starting\ glass}}{\rho_i} \quad (2)$$

Peak area of Xe K_α fluorescence peak is obtained by integration of peak intensity, considering a linear baseline from 29.2 keV to 30.2 keV. The average density, ρ_i, is calculated using a 3rd order Birch-Murnaghan equation of state assuming ideal mixing of H_2O and silicate melt [35], and the density of crystals using the molar volumes of plagioclase $Ab_{80}An_{20}$ predicted from the Murnaghan equation of state [36], the thermal expansion of plagioclase feldspars [37], and the molar volumes of clinopyroxene calculated from high-T Birch-Murnaghan equation of state of diopside as a proxy [38]. All densities for crystals and melt are summarized in Table 3.

Xenon weight fraction in crystals can finally be obtained from mass balance calculations using phase fractions as determined in section 3.2 below:

$$Xe_i = x_m^i Xe_m + \left(1 - x_m^i\right) Xe_c \tag{3}$$

where Xe_m is the Xe weight fraction in the melt, Xe_c, the Xe weight fraction in crystals, and x_m^i, the melt fraction in pattern i. At each P-T point, Xe_m is taken from pure melt pattern except for one P-T condition (run HH355 1.6 GPa-700°C) for which we did not succeed to localize a pure melt zone, and had to solve a set of two mass-balance equations, one for the crystal-rich zone and one for the melt-rich zone.

If Xe concentrations in each phase are not needed, Xe partition coefficient can be obtained without using fluorescence data on the fully molten sample, hence without doing any assumption on negligible cell-assembly deformation upon cooling from fully molten state. In that case, one can combine equations 1 and 3 to directly calculate Xe partition coefficient from Xe fluorescence line area measured on co-existing melt and crystal-rich areas (equation 4). The contribution from cell-assembly is exactly the same in co-existing melt and crystal-rich areas since they are collected at the same P-T condition, and consequently cancels out.

$$\begin{aligned} D_{crystal/melt} &= \frac{Xe_c}{Xe_m} \\ &= \frac{(Xe_i - x_m Xe_m)/(1 - x_m)}{Xe_m} \\ &= \frac{(peak\ area)_i/\rho_i - (x_m(peak\ area)_m/\rho_m)/(1 - x_m)}{(peak\ area)_m/\rho_m} \end{aligned} \tag{4}$$

Overall, the largest source of uncertainty stems from the noise/signal ratio on Xe K_α fluorescence peak (between 4% and 16% error bar, depending on EDX averaged pattern). Additional sources of uncertainty are: 1) uncertainty on *P-T* conditions that translate into approximately 1% error bar on phases densities, and 2) in the case of Xe concentration in crystals, uncertainty on phase fractions (see section 3.2 below), also stemming from the noise/signal ratio on XRD spectra (4% to 8%). Error bars given in Table 3 result from the propagation of these uncertainties.

3.2 Determination of phase fractions

To obtain phase fractions for patterns collected on mixture of crystals and melts, angle-dispersive diffraction data (DAC experiments) are processed by LeBail refinement (supplementary Fig.S6), adopting the procedure developed by Madsen et al. [39] for crystallinity quantification which relies on the proportionality between (a) amorphous (*i.e.* molten) fraction and measured amorphous intensity; (b) crystalline fraction and measured crystalline intensity. In the case of resistive-heating DAC experiments, crystals remained small enough to produce powder-quality X-ray diffraction patterns (supplementary Fig.S7). The weight fraction of crystals is thus obtained from the ratio of cristalline intensity to cristalline+melt intensity (*i.e.* diffuse scattering), and reciprocally for the weight fraction of melt.

During large volume press experiments, crystals grew to a larger size than in DAC, resulting in preferred orientation as can be seen from SEM images of recovered quenched samples (Fig.1d). In that case, we cannot rely on measured crystalline intensity. Instead, melt phase proportion was obtained from the ratio between diffuse melt intensity in a given EDX pattern and that observed for pure melt pattern, both after subtraction of the background signal taken from EDX pattern collected on

surrounding MgO (supplementary Fig. S8). For that purpose, diffraction signal was processed by normalizing intensities by time and slits size, and converting energy to scattering vector, $q = Esin\theta/hc$, where E is the photon energy, 2θ, the scattering angle, h, the Planck constant, and c, the speed of light. Crystal fraction is then obtained by difference to 100%. This method was cross-checked for two samples by image processing of X-ray tomography scans (cf section 2.4) on two recovered diamond capsules (runs HH355 and HH357) extracted from the cell-assembly, assuming that crystal *vs* melt fractions are not affected by the quenching process. The data were processed with ImageJ software for 3-D reconstruction (Fig. 4) [40]. After that, melt and crystals phase fractions were calculated for each beam path as defined by the position of collimating slits recorded on X-ray radiographs during *in situ* EDX experiments (Fig. 4c and 4d).

The results obtained using both X-ray tomography and intensity ratio calculation of EDX data tested on run HH355 are within the 8% uncertainty, with 73% melt at the melt-rich position and 56% melt at the crystal-rich position (from X-ray tomography) *vs* 68% and 55% respectively (from intensity ratio calculation).

4. Results and discussion

4.1 Results: Xe partitioning behaviour

The higher Xe concentrations are systematically found in crystal phase for clinopyroxene/melt system at all investigated *P-T* conditions, indicating Xe preferentially goes into clinopyroxene rather than into the melt (Fig. 5 and 6, and Table 3). Our *in situ* high *P-T* measurements thus show that Xe is a compatible

element in clinopyroxene at depth with $D^{Xe}_{clinopyroxene/melt}$ reaching 3.58 ± 0.93 at 700°C, and linearly decreasing with increasing *T* (Fig.6 and Table 3). Only one data point is collected for plagioclase/melt system using DAC, at the highest *T* investigated (1010 °C), with higher Xe content retained in melt. Consequently, for plagioclase/ melt system, Xe is found to preferentially partition into the melt ($D^{Xe}_{plagioclase/melt}$ = 0.50 ± 0.10) at 1010 °C. Note that this lower value is consistent with the negative *T*-trend that we report for Cpx/melt partitioning (Fig.6).

These results are two orders of magnitude below the upper range of former Xe partitioning studies on olivine/melt and clinopyroxene/melt systems (Fig. 5) but clearly near/above unity, implying that one cannot systematically discard Xe bubbles in quenched samples as those must have at least partly been formed upon quenching to ambient conditions. In the case of Xe reactivity with olivine at high *P*-*T* conditions through Xe substitution to Si [41], Xe was indeed observed to be at least partly released from crystals upon quenching to room *T* as indicated by the appearance of pure Xe diffraction signal [42].

Noble gases retention sites in silicate melts are inside rings and cavities of the three-dimensional network. Their solubility depends on the melt composition and structure, it increases with the SiO_2 content and with *P* up to approximately 5 GPa but is independent on *T* for Ar and Xe [19,20]. Xe-O bonds have been reported to form in hydrous silica-rich melts when compressed with a coordination number of about 12, consistent with Xe insertion in the most abundant 6-membered rings [13]. However, the Xe-O coordination number shows no dependence on either *T* or *P* at the experimental conditions. Consequently, Xe solubility in melts cannot be simply

explained by Langmuir adsorption model. On the other hand, Xe reacts with minerals by substituting to Si, bonding to either 4 oxygen atoms in silica polymerized phases [43] or to 3 oxygen atoms in olivine depolymerized structure [41], with oxidation state between + 2 and + 3. Yet there is so far no data about the exact oxidation state of Xe in magmas.

Xenon solubility is promoted by the existence of Si-vacancies in quartz [10] and olivine, owing for the latter to an increased concentration of Fe^{3+} cations at the high experimental *T* [44]. Based on the EPMA analyses on quenched samples (Table 2), less Al^{3+} is retained in clinopyroxene when *T* increases, and it results in the lack of the vacancy-forming element in clinopyroxene. In consequence, the crystal could retain less Xe. Therefore, we suggest the negative relationship between $D^{Xe}_{c/m}$ and *T* (Fig.6) is due to the decrease of trivalent elements in clinopyroxene phase.

4.2 Xe storage in the deep crust and the missing Xe

Xenon can be stored within major minerals of the deep continental crust [10,48] and upper mantle [16,45]. Xenon crystal/melt partition coefficients obtained from our experiments (0.50±0.10 to 3.58±0.93) indicate that Xe is moderately incompatible to compatible at continental *P-T* conditions. This range of values confirms the compatibility of Xe in minerals. Xenon compatibility in crystalline silicates at depth is attributed to its *P*-induced chemical reactivity, with the formation of Xe-O bonds [10,41,43]. This short bond length is due to Xe being oxidized, not neutral. Compared to other noble gases, Xe is therefore preferentially retained into the crystal fraction during partial melting processes, rather than degassed from the melt. Xenon is recycled at depth by subduction processes, leading to the mantle noble gas isotopic

composition [45]. Besides, Xe is detected up to 0.2 ppb (part per billion) in deep sea siliceous fossils [46], that eventually also are recycled into the mantle at subduction zones. In the case of haplogranite, Xe degasses strongly or is preferentially retained within the haplogranitic melt, depending on *T* [10]. Thus, in the presence of aqueous fluids, Xe is not necessarily degassed upon rock melting. Xenon stored or recycled at depth is expected to be only partially released during partial melting process, and mostly remains in crustal minerals with upwelling of magma. Thus, our results support the hypothesis of Xe storage in the continental crust. This is consistent with natural Xe enrichments of 1 to 3 orders of magnitude compared to krypton (Kr) that have been reported in exhumed Red Rock granite ($^{130}Xe/^{84}Kr \sim 0.2$) from the Sudbury structure, Canada, formed by an asteroid impact [47] and in North America tektites ($^{130}Xe/^{84}Kr \sim 0.5$) [48]. While in common rocks, $^{130}Xe/^{84}Kr$ is 0.004-0.012 in granites [47] and 0.007-0.033 in igneous rocks [49]. The time scale is very different between natural shocked rocks and slowly exhumed ones that likely underwent episodes of metamorphism/magmatism resulting in Xe loss. Thus, only shocked rocks, and to lesser extent fast ascent rocks (*e.g.*, xenoliths) may preserve Xe excess.

As a matter of fact, our experimental conditions are restricted to a simple system of crystal/silica-rich melt. This type of investigation must now be extended to mantle/ oceanic compositions, *i.e.* more basaltic systems, to explore the potential of the upper mantle to store Xe at depth as natural Xe excesses have also been reported in xenoliths [50-52].

4.3 Advantages of the new EDX protocol for in situ partitioning experiments

For the angle-dispersive set-up, the volume sampled by XRF is slightly smaller than the volume probed by XRD, and great care must be taken to align the XRF detector with the XRD focal point (Fig. 7a). While for the energy-dispersive set-up, both structural information (*i.e.* diffraction) and chemical information (*i.e.* fluorescence) are collected using one single detector with the exact same gauge volume and geometry of sample probed (Fig. 7b). The obtained diffraction pattern is therefore more accurate.

Another disadvantage of the ADX set-up is that fluorescence signal scattered from sample environment (*e.g.* diamond anvils, rhenium gasket, body cell) is also detected, which can impede detection of some elements at low concentrations. This problem is circumvented in the EDX set-up due to the collimation tip placed in front of the Ge-detector. Note that the situation can be improved with an ADX set-up by placing an additional polycapillary X-ray half-lens in front of the fluorescence detector [53].

To evaluate the consistency between the two data processing methods (*i.e.* PyMCA software and equations 1-4 following Simabuco and Nascimento [35]), both of them have been tested on the DAC fluorescence data, and results are consistent (cf Table 3 and Fig. 6). Thus, the feasibility of the new protocol is demonstrated, with advantages of the congruent geometry of sample probed.

In terms of limitations, the lowest Xe content measured here is 0.013±0.002 wt%. This could be achieved by inserting boron-epoxy window along the X-ray path (see section 2.3), which significantly reduced signal absorption by surrounding materials (see Fig.3a). This step is however not necessary for Xe content at the 0.1 wt% level.

This new technique therefore offers a new avenue to determine elements concentration, including for volatile elements, in phases using X-ray fluorescence signal on energy dispersive diffraction data. Besides, by using large volume press instead of resistive-heating DAC, this protocol allows to probe geological systems at higher *P-T* conditions, with potential for significant impact in the experimental petrology and Earth's sciences community. Higher *P-T* conditions can be achieved in laser heated DACs. However while the whole sample is at constant *T* in a resistive heated DAC, only the central part of the laser heated spot is homogeneous for *T* in a laser heated DAC, making equilibrium measurements between co-existing phases very challenging [54]. The present method is nonetheless restricted to the investigation of elements with fluorescence signal between 15 keV and 120 keV for most synchrotron sources.

Acknowledgements

We acknowledge I. Esteve and S. Delbrel for assistance with the SEM analyses, K. Beneut for assistance with the Raman spectroscopy platform at IMPMC, N. Rividi for assistance with the EPMA (Camparis platform, Sorbonne Université), and M. Bellato for assistance at the micro-CT scan facilities at the National Museum of Natural History in Paris (AST-RX). Parts of this research were carried out at beamline P02.2 and beamline P61B at DESY, a member of the Helmholtz Association (HGF). The research leading to this result has been supported by the project CALI1PSOplus under the Grant Agreement 730872 from the EU Framework Programme for Research and Innovation HORIZON 2020. The SEM facility of IMPMC is supported by Région Ile de France Grant SESAME 2006 NOI-07-593/R, INSU-CNRS, INP-CNRS, Sorbonne Université, and by the French National Research Agency (ANR) Grant ANR-07-BLAN-0124-01. Q. C. is funded by the China Scholarship Council (#201806340094).

References

[1] Staudacher T, Allègre CJ. Terrestrial xenology. Earth and Planetary Science Letters. 1982;60:389-406

[2] Pepin RO. Atmospheres on the terrestrial planets: Clues to origin and evolution. Earth and Planetary Science Letters. 2006;252:1-14.

[3] Allègre CJ, Staudacher T, Sarda P, Kurz M. Constraints on evolution of Earth's mantle from rare gas systematics. Nature. 1983; 303:762-6.

[4] Gonnermann HM, Mukhopadhyay S. Preserving noble gases in a convecting mantle. Nature. 2009;459:560-3.

[5] Bowyer TW, Schlosser C, Abel KH et al. Detection and analysis of xenon isotopes for the comprehensive nuclear-test-ban treaty international monitoring system. Journal of environmental radioactivity. 2002;59:139-51.

[6] Anders E, Owen T. Mars and Earth: Origin and abundance of volatiles. Science. 1977;198:453-65.

[7] Ozima M, Podosek F. Formation age of Earth from $^{129}I/^{127}I$ and $^{244}Pu/^{238}U$ systematics and the missing Xe. Journal of Geophysical Research: Solid Earth. 1999;104:25493-9.

[8] Zahnle KJ, Gaseca M. and Catling DC. Strange messenger: A new history of hydrogen on Earth, as told by xenon. Geochim. Cosmochim. Acta. 2018;244:56–85.

[9] Avice, G, Marty B, Burgess R et al. Evolution of atmospheric xenon and other noble gases inferred from Archean to Paleoproterozoic rocks. Geochim. Cosmochim. Acta. 2018;232:82-100.

[10] Probert MIJ. An ab initio study of xenon retention in α-quartz. Journal of physics: Condensed matter. 2009;22:025501

[11] Kalinowski J, Räsänen M, Gerber RB. Chemically-bound xenon in fibrous silica. Physical Chemistry Chemical Physics. 2014;16:11658-61.

[12] Sanloup C. Noble Gas Reactivity in Planetary Interiors. Frontiers in Physics. 2020;8.

[13] Leroy C, Bureau H, Sanloup C et al. Xenon and iodine behaviour in magmas. Earth and Planetary Science Letters. 2019;522:144-54.

[14] Hiyagon H, Ozima M. Partition of noble gases between olivine and basalt melt. Geochimica et Cosmochimica Acta. 1986;50:2045-57.

[15] Broadhurst CL, Drake MJ, Hagee BE, Bernatowicz TJ. Solubility and partitioning of Ne, Ar, Kr and Xe in minerals and synthetic basaltic melts. Geochimica et Cosmochimica Acta. 1992;56:709-23.

[16] Heber VS, Brooker RA, Kelley SP, Wood BJ. Crystal–melt partitioning of noble gases (helium, neon, argon, krypton, and xenon) for olivine and clinopyroxene. Geochimica et Cosmochimica Acta. 2007;71:1041-61.

[17] Clarke FW, Washington HS. The composition of the earth's crust: US Government Printing Office; 1924.

[18] Boettcher SL, Guo Q., Montana A. A simple device for loading gases in high-pressure experiments. American Mineralogist. 1989;74:1383-4.

[19] Schmidt BC, Keppler H. Experimental evidence for high noble gas solubilities in silicate melts under mantle pressures. Earth and Planetary Science Letters. 2002;195:277-90.

[20] Carroll MR, Stolper EM. Noble gas solubilities in silicate melts and glasses: New experimental results for argon and the relationship between solubility and ionic porosity. Geochimica et Cosmochimica Acta. 1993;57:5039-51.

[21] Boehler R, De Hantsetters K. New anvil designs in diamond-cells. High Pressure Research. 2004;24:391-6.

[22] Fei Y, Mao H-k. In situ determination of the NiAs phase of FeO at high pressure and temperature. Science. 1994;266:1678-80.

[23] Fei Y, Ricolleau A, Frank M, et al. Toward an internally consistent pressure scale. Proceedings of the National Academy of Sciences. 2007;104:9182-6.

[24] Bureau H, Auzende AL, Marocchi M et al.. Modern and past volcanic degassing of iodine. Geochimica et Cosmochimica Acta. 2016;173:114-25.

[25] Hammersley A. computer program FIT2D. ESRF, Grenoble. 1998.

[26] Rodríguez-Carvajal J. Recent advances in magnetic structure determination by neutron powder diffraction. Physica B: Condensed Matter. 1993;192:55-69.

[27] Dewaele A, Fiquet G, Andrault D, et al. P−V−T equation of state of periclase from synchrotron radiation measurements. Journal of Geophysical Research: Solid Earth. 2000;105:2869-77.

[28] Montana A, Guo Q, Boettcher S et al. Xe and Ar in high-pressure silicate liquids. American Mineralogist. 1993;78:1135-42.

[29] Leroy C, Sanloup C, Bureau H et al. Bonding of xenon to oxygen in magmas at depth. Earth and Planetary Science Letters. 2018;484:103-10.

[30] Shimada M. Melting of Albite at high pressures. Journal of Physics of the Earth. 1972;20, 59-70.

[31] Bell PM, Davis BT. Melting relations in the system jadeite-diopside at 30 and 40 kilobars. Am J Sci. 1969;267:17-32.

[32] Crépisson C. 'Missing Xenon': experimental and theoretical study of Xe storage in crustal and upper mantle minerals: Sorbonne université; 2018.

[33] Solé VA, Papillon E, Cotte M et al. A multiplatform code for the analysis of energy-dispersive X-ray fluorescence spectra. Spectro. Acta Part B. 2007;62:63-8.

[34] Simabuco S, Nascimento Filho V. Quantitative analysis by energy dispersive X-ray fluorescence by the transmission method applied to geological samples. Scientia Agricola. 1994;51:197-206.

[35] Malfait WJ, Seifert R, Petitgirard S et al. The density of andesitic melts and the compressibility of dissolved water in silicate melts at crustal and upper mantle conditions. Earth Planet. Sci. Lett.. 2014;393:31-8.

[36] Holland TJB, Powell R. An internally consistent thermodynamic data set for phases of petrological interest. Journal of metamorphic Geology. 1998;16:309-43.

[37] Tribaudino M, Angel RJ, Cámara F, et al. Thermal expansion of plagioclase feldspars. Contributions to Mineralogy and Petrology. 2010;160:899-908.

[38] Zhao Y, Von Dreele RB, Shankland TJ, et al.. Thermoelastic equation of state of jadeite NaAlSi2O6: An energy−dispersive Reitveld Refinement Study of low symmetry and multiple phases diffraction. Geophysical Research Letters. 1997;24:5-8

[39] Madsen IC, Scarlett, NVY and Kern A. Description and survey of methodologies for the determination of amorphous content via X-ray powder diffraction. Z. Krist.-Cryst. Mater. 2011;226:944-955.

[40] Abràmoff MD, Magalhães PJ, Ram SJ. Image processing with ImageJ. Biophotonics international. 2004;11:36-42.

[41] Crépisson C, Blanchard M, Lazzeri M et al. New constraints on Xe incorporation mechanisms in olivine from first-principles calculations, Geochim. Cosmochim. Acta. 2018; 222:146–155.

[42] Sanloup C, Schmidt B, Gudfinnsson G et al. Xenon and Argon: A contrasting behavior in olivine at depth. Geochimica et Cosmochimica Acta. 2011;75:6271-84.

[43] Crepisson C, Sanloup C, Blanchard M et al. The Xe-SiO_2 system at moderate pressure and high temperature. Geochemistry, Geophysics, Geosystems. 2019;20:992-1003.

[44] Mackwell SJ, Dimos D, Kohlstedt DL. Transient creep of olivine: point-defect relaxation times. Philosophical Magazine A. 1988;57:779-89.

[45] Holland G, Ballentine CJ. Seawater subduction controls the heavy noble gas composition of the mantle. Nature. 2006;441:186-91.

[46] Matsuda JI, Matsubara K. Noble gases in silica and their implication for the terrestrial 'missing' Xe. Geophys. Res. Lett. 1989;16:81–84.

[47] Kuroda PK, Sherrill RD, Jackson KC. Abundances and isotopic compositions of rare gases in granites. Geochemical Journal. 1977;11, 75-90.

[48] Palma RL, Rao MN, Rowe MW, Koeberl C. Krypton and xenon fractionation in North American tektites. Meteoritics & Planetary Science. 1997;32:9-14.

[49] Miura Y, Nagao K. Noble gases in six GSJ igneous rock samples. Geochemical Journal. 1991;25:163-71.

[50] Hennecke EW, Manuel O. Noble gases in an Hawaiian xenolith. Nature. 1975;257:778-80.

[51] Poreda R, Farley K. Rare gases in Samoan xenoliths. Earth and Planetary Science Letters. 1992;113:129-44.

[52] Czuppon G, Matsumoto T, Handler MR, Matsuda J-i. Noble gases in spinel peridotite xenoliths from Mt Quincan, North Queensland, Australia: undisturbed

MORB-type noble gases in the subcontinental lithospheric mantle. Chemical Geology. 2009;266:19-28.

[53] Wilke M, Appel K, Vincze L et al. A confocal set-up for micro-XRF and XAFS experiments using diamond-anvil cells. J. Synch. Rad. 2010;17:669-675.

[54] Petitgirard S, Borchert M, Andrault D et al. An in situ approach to study trace element partitioning in the laser heated diamond anvil cell. Rev. Sci. Instr. 2012;83:013904.

Table 1. Experimental conditions.

Run	*P* (GPa)	*T* (°C)	Duration (h)	Fluorescence collection time	State
Cell5	2[a]	1010[a]	6.5	30 min melt, 30 min crystals	melt + plagioclase
HH354	3.5	25	7.5	1h36	starting glass
	3.2	800		1 min	fully crystalline
	2.5	800		1 min	fully crystalline
	1.7	1000		9 min	melt
	1.8[a]	950[a]		1h33 melt, 50 min crystals	melt + jadeite
HH355	2.8	950	15	1 min	fully crystalline
	1.4	950		3 min	melt + jadeite
	2.1	1050		1h40	melt
	1.7	800		1 min	melt + jadeite
	1.6[a]	700[a]		1h47 melt, 1h58 crystals	melt + jadeite
HH357	2.0	25	14.5	2h32	starting glass
	2.3	700		1 min	fully crystalline
	2.0	800		1 min	fully crystalline
	1.1	850		21 min	melt
	1.7[a]	850[a]		2h26 melt, 2h55 crystals	melt + omphacite

Run Cell5 was conducted in DAC; Runs HH354 to 357 were conducted in LVP; # = number of scans; Duration = duration of the run at high-*T*; [a], quenched *P*-*T* conditions; uncertainty on *P* is 0.3 GPa, on *T* is 50 °C. Note that run HH355 is the next-day continuation of run HH354.

Table 2. Chemical analyses on starting glasses and recovered high *P-T* samples in wt% obtained from EPMA. Analyses are based on 10-20 data points, in brackets: standard deviation.

	Na_2O	SiO_2	CaO	Al_2O_3	MgO	Xe	H_2O*	total
$Ab_{80}An_{20}$	8.64 (0.47)	62.82 (0.46)	4.47 (0.08)	25.45 (0.39)				101.41
PC162a[1]	4.92 (0.19)	57.63 (1.48)	3.71 (0.13)	21.94 (0.62)		0.14 (0.01)	10.89 (1.37)	99.23
PC162b[1]	4.98 (0.27)	56.74 (0.77)	3.42 (0.15)	20.51 (0.32)		0.02 (0.01)	12.02 (1.50)	97.69
HH355m[2]	4.84 (0.57)	66.80 (2.02)	1.22 (0.12)	14.80 (0.67)	0.01 (0.01)	0.05 (0.01)	10.76 (1.57)	98.49
HH355c[2]	7.76 (1.02)	54.99 (0.95)	11.86 (1.91)	23.23 (1.82)	4.94 (1.35)	< DL		102.78
HH357m[2]	7.72 (0.98)	60.08 (0.99)	2.46 (0.12)	17.52 (0.46)	1.02 (0.15)	< DL	11.66 (1.07)	100.46
HH357c[2]	6.81 (0.96)	55.57 (1.11)	13.45 (1.3)	18.57 (0.94)	8.37 (0.8)	< DL		102.77
Cell5m[3]	7.55 (0.73)	63.46 (0.95)	4.50 (0.19)	24.04 (0.58)		0.14 (0.01)		99.75

$Ab_{80}An_{20}$ is the dry starting glass; [1]: hydrated glasses from piston cylinder runs, [2]: samples recovered from *in situ* LVP experiments, [3]: sample recovered from *in situ* DAC experiment; H_2O* is estimated from Raman spectra (see Supplemental file for details); m = melt; c = crystal; DL = detection limit (230-260 ppm).

Table 3. Phase proportions, phase densities, Xe weight fractions, and Xe partition coefficients.

Run	starting glass	P	T	Density (g/cm^3)		melt -rich	crystal-rich	Xe_c	$Xe_{m/g}$	$D^{Xe}_{crystal/melt}$
		(GPa)	(°C)	ρ_c	$\rho_{m/g}$	x_m	x_m	(wt%)	(wt%)	
HH354	PC162a	1.8	950	3.264	2.253	100	82	0.204 (0.031)	0.125 (0.010)	1.63 (0.37)
HH355	PC162a	1.6	700	3.288	2.252	73	56	0.222 (0.038)	0.062 (0.006)	3.58 (0.93)
HH357	PC162b	1.7	850	3.273	2.216	95	77	0.033 (0.008)	0.013 (0.002)	2.54 (0.97)
Cell5	PC162a	2.0	1010	2.518	2.267	97	57	0.110 (0.009)	0.144 (0.006)	0.76 (0.14)
		2.0	1010	2.518	2.267	97	57	0.074[a] (0.007)	0.148[a] (0.009)	0.50[a] (0.11)

x_m , melt % fraction; Xe_c, Xe content in crystal; $Xe_{m/g}$, Xe content in melt or glass; uncertainties (in brackets); [a], calculated with PyMCA software. Note that melt fraction in 'crystal-rich' area, being determined locally, does not necessarily increases with T unlike the total fraction of melt in the sample.

Fig. 1

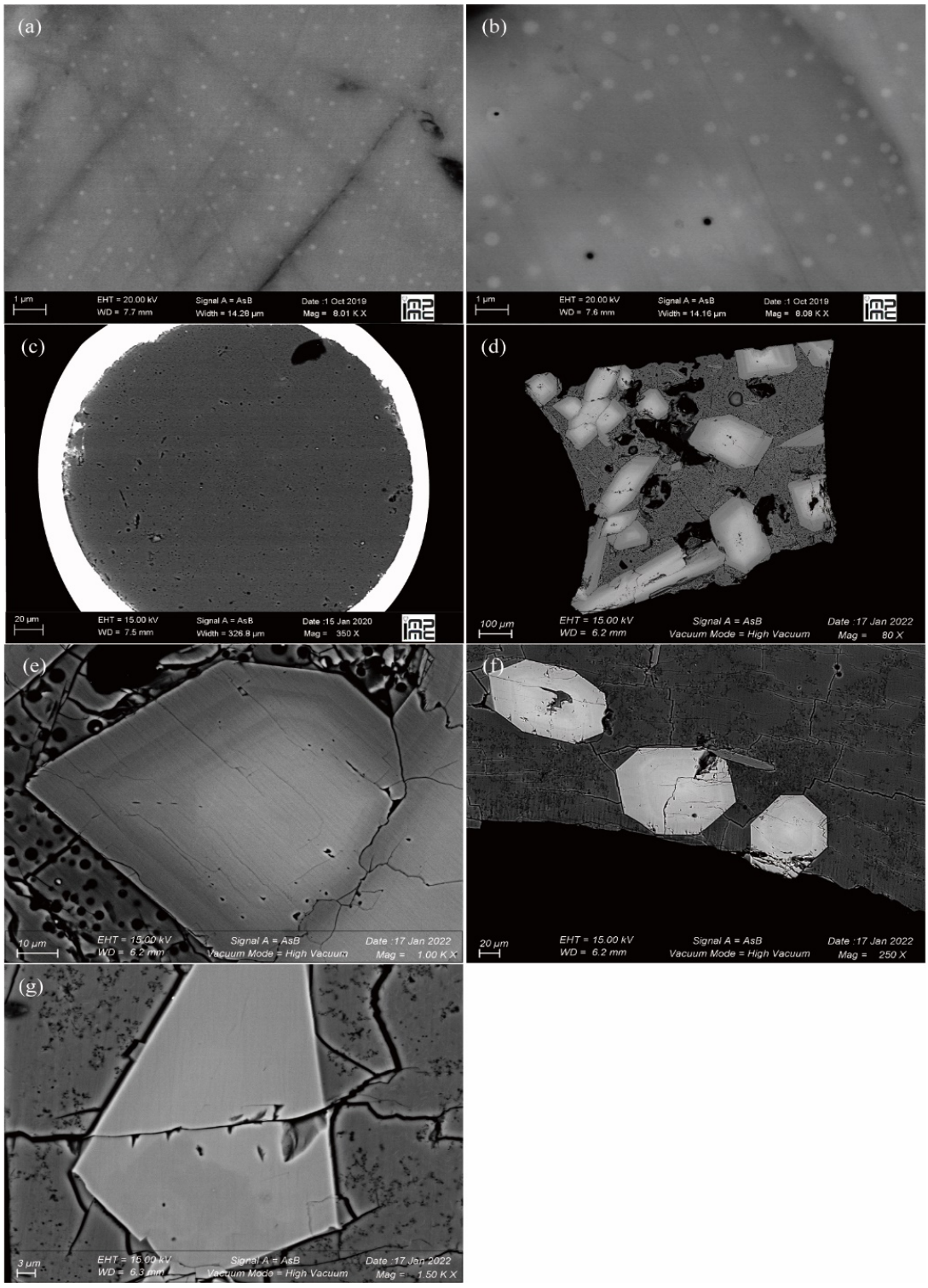
(a)
1 µm
EHT = 20.00 kV
WD = 7.7 mm
Signal A = AsB
Width = 14.28 µm
Date :1 Oct 2019
Mag = 8.01 K X
(b)
1 µm
EHT = 20.00 kV
WD = 7.6 mm
Signal A = AsB
Width = 14.16 µm
Date :1 Oct 2019
Mag = 8.08 K X
(c)
20 µm
EHT = 15.00 kV
WD = 7.5 mm
Signal A = AsB
Width = 326.8 µm
Date :15 Jan 2020
Mag = 350 X
(d)
100 µm
EHT = 15.00 kV
WD = 6.2 mm
Signal A = AsB
Vacuum Mode = High Vacuum
Date :17 Jan 2022
Mag = 80 X
(e)
10 µm
EHT = 15.00 kV
WD = 6.2 mm
Signal A = AsB
Vacuum Mode = High Vacuum
Date :17 Jan 2022
Mag = 1.00 K X
(f)
20 µm
EHT = 15.00 kV
WD = 6.2 mm
Signal A = AsB
Vacuum Mode = High Vacuum
Date :17 Jan 2022
Mag = 250 X
(g)
3 µm
EHT = 15.00 kV
WD = 6.3 mm
Signal A = AsB
Vacuum Mode = High Vacuum
Date :17 Jan 2022
Mag = 1.50 K X

Fig. 2

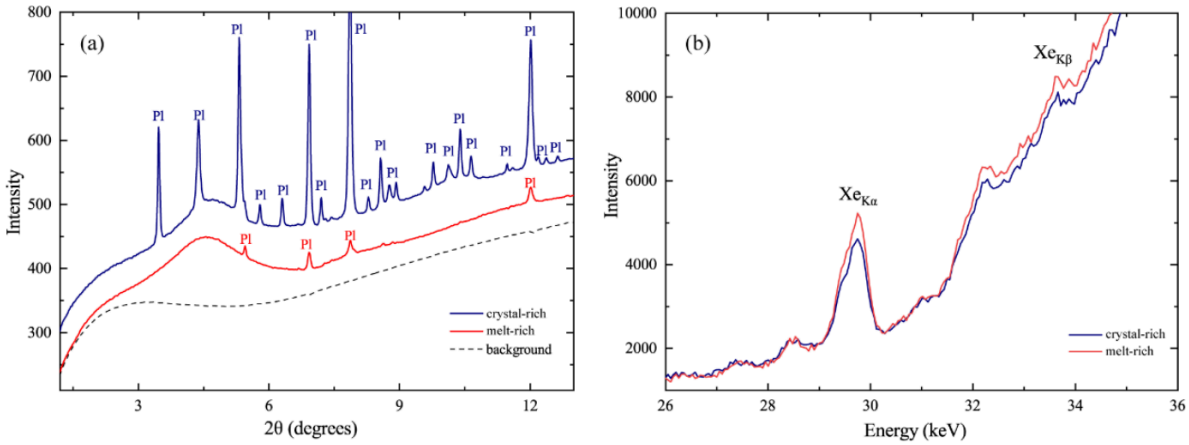
(a)
Intensity
2θ (degrees)
Pl
crystal-rich
melt-rich
background
(b)
Intensity
Energy (keV)
$Xe_{K\alpha}$
$Xe_{K\beta}$
crystal-rich
melt-rich

Fig. 3

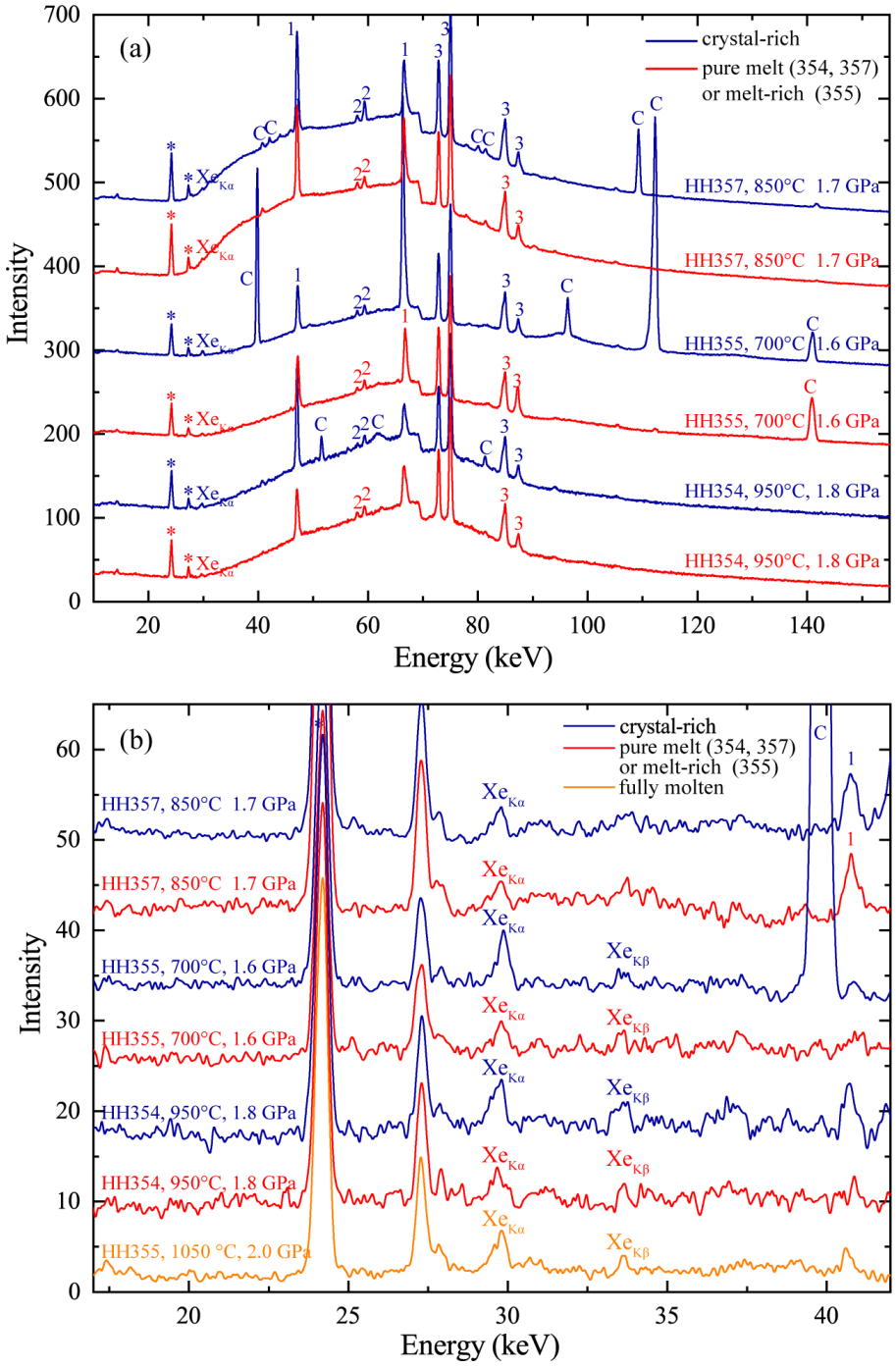
(a)
crystal-rich
pure melt (354, 357)
or melt-rich (355)
HH357, 850°C 1.7 GPa
HH357, 850°C 1.7 GPa
HH355, 700°C 1.6 GPa
HH355, 700°C 1.6 GPa
HH354, 950°C, 1.8 GPa
HH354, 950°C, 1.8 GPa
Intensity
Energy (keV)
(b)
crystal-rich
pure melt (354, 357)
or melt-rich (355)
fully molten
HH357, 850°C 1.7 GPa
HH357, 850°C 1.7 GPa
HH355, 700°C, 1.6 GPa
HH355, 700°C, 1.6 GPa
HH354, 950°C, 1.8 GPa
HH354, 950°C, 1.8 GPa
HH355, 1050 °C, 2.0 GPa
Intensity
Energy (keV)

Fig. 4

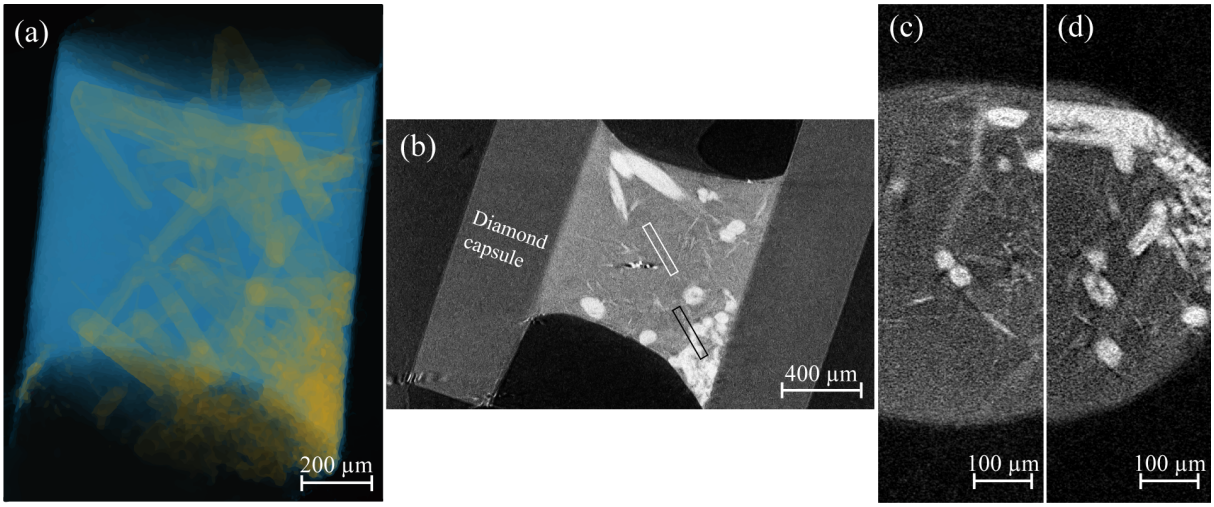
(a)
200 µm
(b)
Diamond capsule
400 µm
(c)
100 µm
(d)
100 µm

Fig. 5

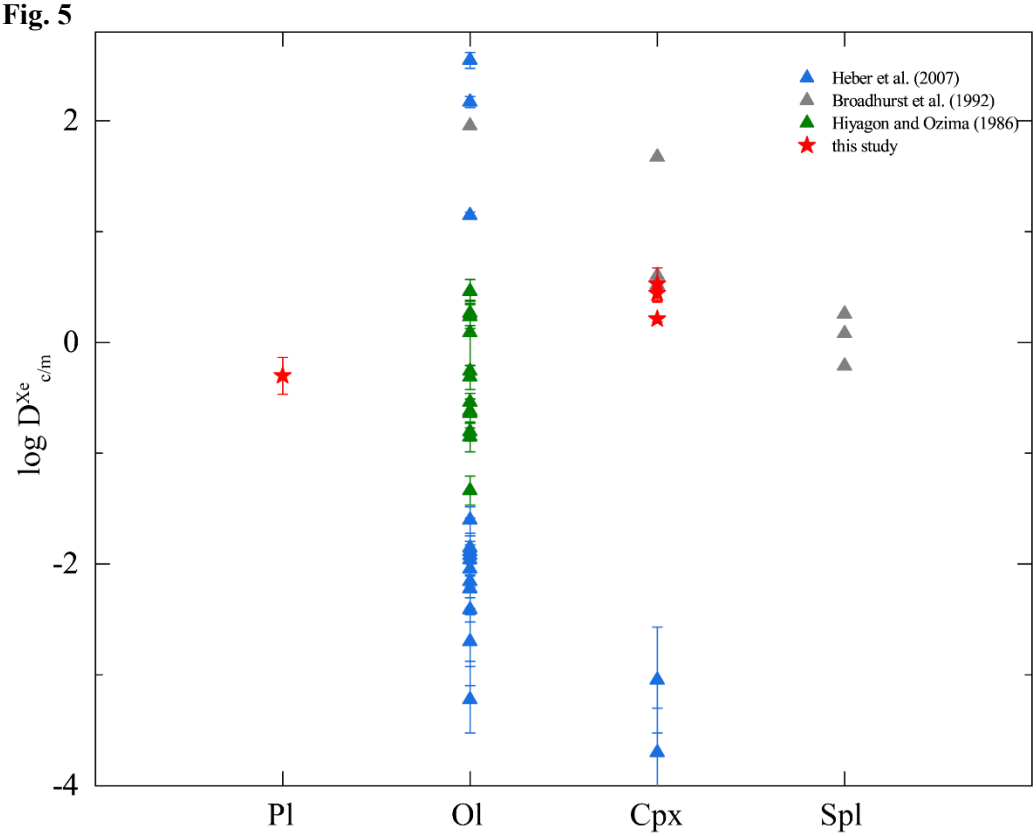
Heber et al. (2007)
Broadhurst et al. (1992)
Hiyagon and Ozima (1986)
this study
log D^Xe c/m
2
0
-2
-4
Pl
Ol
Cpx
Spl

Fig. 6

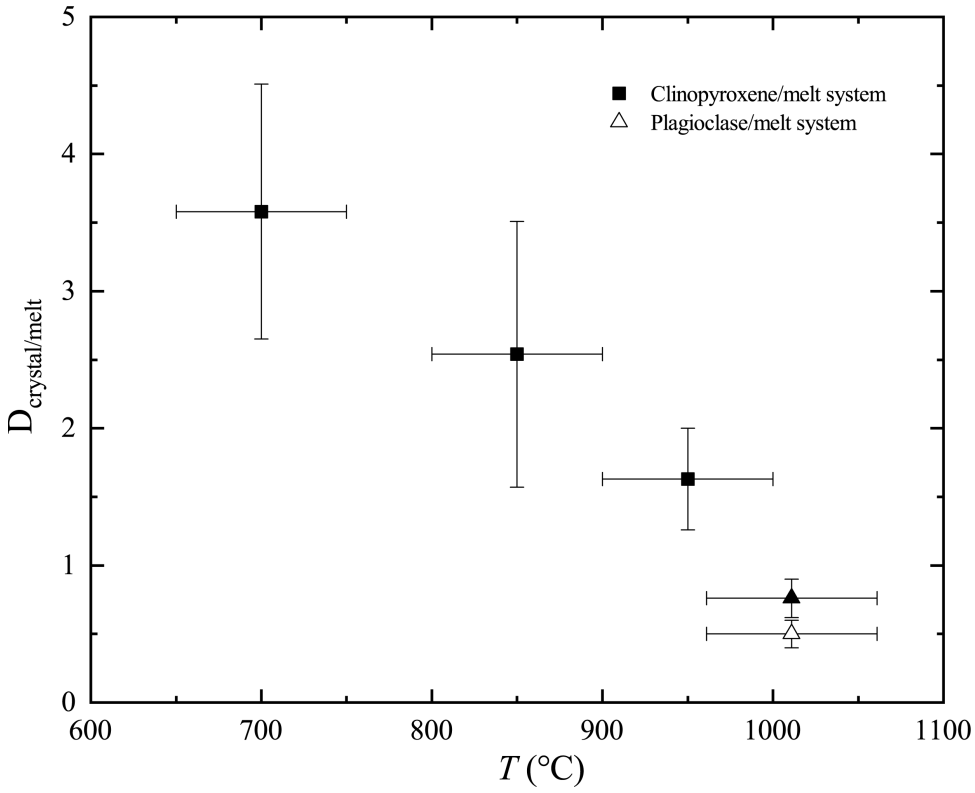
Clinopyroxene/melt system
Plagioclase/melt system
$D_{crystal/melt}$
T (°C)
0
1
2
3
4
5
600
700
800
900
1000
1100

Fig. 7

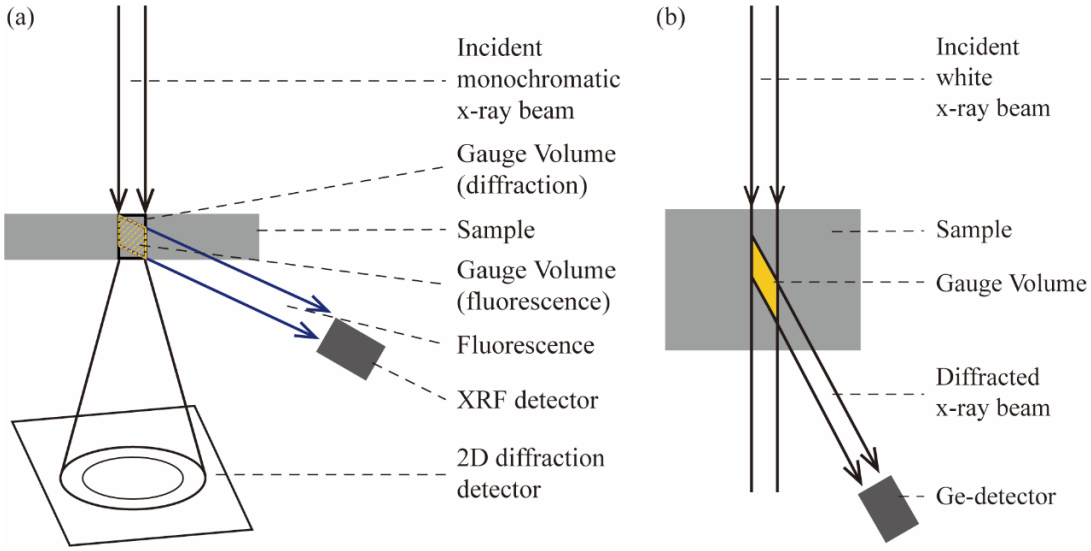
(a)
Incident monochromatic x-ray beam
Gauge Volume (diffraction)
Sample
Gauge Volume (fluorescence)
Fluorescence
XRF detector
2D diffraction detector
(b)
Incident white x-ray beam
Sample
Gauge Volume
Diffracted x-ray beam
Ge-detector

Fig. 1. SEM images of starting materials and high *P-T* quenched samples. Starting glasses PC162a (a) and PC162b (b); bright dots may indicate Ca-rich plagioclase seeds. (c) Quenched sample Cell5 from DAC experiments surrounded by Re gasket (bright periphery); quenched sample is mostly glass, with a few plagioclase crystals near the gasket edge. (d) Quenched sample HH355 from LVP experiment; (e) zoomed on clinopyroxene crystal; holes are assumed to be H_2O and CH_4 bubbles open upon polishing. (f) Quenched sample HH357 and (g) zoomed on clinopyroxene crystal; grey area is melt while brighter areas are clinopyroxene crystals (Ca-rich core and Na-rich rims); black dots in the glass are graphite crystals; about 2% alumina silicate (columnar crystals) is detected.

Fig. 2. (a) Angle-dispersive X-ray diffraction data collected at 2 GPa and 1010 °C in resistive-heating diamond-anvil cell (run Cell5); (b) corresponding X-ray fluorescence spectra. Pl, plagioclase; dotted line: background obtained using an empty gasket in the DAC. The Xe K_α and K_β fluorescence rays are observed at 29.78 keV and 33.62 keV, respectively.

Fig. 3. Full i*n situ* energy-dispersive spectra data-set from large-volume press experiments. (a) Data on coexisting melt (red lines) and crystal-rich (blue lines) areas for all three LVP runs; the increased intensity between 25 keV and 60 keV for run HH357 is due to the use of a boron-epoxy window along the X-ray path that significantly reduced signal absorption by the surrounding materials; (b) zoom on Xe fluorescence signal for all three data-sets and fully molten pattern (orange line) collected at high *P* for run HH355, after subtraction of a linear baseline. *, Ge fluorescence from detector; 1, MgO diffraction from cell-assembly; 2, W fluorescence 3, Pb fluorescence from beamline elements, and the W absorption edge is visible at 69 keV; C, crystalline diffraction peaks. Due to the large crystal sizes (cf Fig. 1), not all diffraction peaks are observed on crystal-rich patterns but only a few depending on crystal orientation.

Fig. 4. X-ray tomography slice reconstruction on the recovered large-volume press sample (HH357). (a) Crystallized omphacite (yellow) coexisting with partial melt quenched as a glass (blue); (b) recovered sample with the beam slits position on melt-rich (white rectangle) and crystal-rich areas (black rectangle); reconstructed cross sections at (c) ‘melt-rich’ and (d) ‘crystal-rich’ positions.

Fig. 5. Crystal-melt partitioning coefficients of Xe. From our experiments (red stars) and compared with literature data. Pl, plagioclase; Ol, olivine; Cpx, clinopyroxene; Spl. spinel.

Fig. 6. Temperature effect on Xe crystal/melt partitioning under *P*. Solid symbols: $D^{Xe}_{c/m}$ obtained using method from Simabuco and Nascimento (1994); empty symbols: using method from Solé et al. (2007).

Fig. 7. Schematic geometry of (a) the angle-dispersive X-ray set-up (at P02.2 PETRAIII) and (b) energy-dispersive X-ray set-up (at P61B PETRAIII).